

Voltage-induced suppression of weak localization in graphene

J. Fransson,¹ R. Somphonsane,² H. Ramamoorthy,³ G. He,³ and J. P. Bird^{3,4}

¹*Department of Physics and Astronomy, Uppsala University, Box 516, SE-751 21 Uppsala, Sweden**

²*Department of Physics, King Mongkut's Institute of Technology Ladkrabang, Bangkok 10520, Thailand*

³*Department of Electrical Engineering, University at Buffalo,
the State University of New York, Buffalo, NY 14260-1900, USA*

⁴*Graduate School of Advanced Integration Science, Chiba University, 1-33 Yayoi-cho, Inage-ku, Chiba 263-8522, Japan*

(Dated: February 23, 2017)

In this theoretical study, we explore the manner in which the quantum correction due to weak localization is suppressed in weakly-disordered graphene, when it is subjected to the application of a non-zero voltage. Using a nonequilibrium Green function approach, we address the scattering generated by the disorder up to the level of the maximally crossed diagrams, hereby capturing the interference among different, impurity-defined, Feynman paths. Our calculations of the charge current, and of the resulting differential conductance, reveal the logarithmic divergence typical of weak localization in linear transport. The main finding of our work is that the applied voltage suppresses the weak localization contribution in graphene, by introducing a dephasing time that decreases inversely with increasing voltage.

I. INTRODUCTION

Weak localization is one of longest studied of mesoscopic phenomena, and its discovery in the 1980s provided one of the earliest demonstrations of how transport in disordered conductors may be influenced by phase coherence of the wavefunction [1–3]. Arising from the coherent interference of time-reversed pairs of Feynman paths, which return to their origin after a sequence of elastic scattering events, this *coherent backscattering* enhances the resistance above its Drude value. The size of this quantum correction is governed by the presence of inelastic scattering in the system (such as that which can arise from electron-phonon or quasi-elastic electron-electron interactions), which introduces an effective cut-off in the Feynman-path length for which the coherent backscattering can occur [1]. The weak localization can also be quenched by the application of a magnetic field, which breaks the time-reversal symmetry required for coherent backscattering and generates a negative magneto-resistance. A notable variation on this scenario is provided in systems with strong spin-orbit coupling, in which the additional Berry phase accumulated during backscattering leads to weak antilocalization, the quenching of which in a magnetic field is manifested as a *positive* magneto-resistance [1].

Recently, there has been renewed theoretical [4–10] and experimental [11–22] interest in weak localization, motivated by its various manifestations in graphene. The unusual aspects of the bandstructure of this material, namely its linear dispersion, its equivalent (K and K') valleys, and the chiral nature of its carriers, give rise to a rich variety of phenomena, not normally associated with weak localization in more conventional systems [4]. Also important is the nature of the impurities, or defects, responsible for scattering, with exact backscattering being forbidden for remote impurities that generate long-range scattering [23, 24]. As such, this behavior corresponds to weak antilocalization, in spite of the very weak spin-orbit

coupling intrinsic to graphene. This behavior is modified, however, in the presence of inter-valley scattering generated by short-ranged impurities, and the trigonal warping of the graphene bands. These processes suppress weak antilocalization, and restore the negative magneto-resistance associated with weak localization, the features of which therefore reflect a complex interplay among a number of characteristic scattering times. These effects have now been explored in several experiments [12–14, 17].

Among the large number of studies of weak localization that have been undertaken in graphene, as well as in more conventional materials, the vast majority have focused on inferring information on the localization process from studies of the *linear* conductance. More specifically, most of these works have addressed the manner in which the localization is suppressed by the application of a magnetic field, which breaks time-reversal symmetry and introduces an effective decoherence into electron diffusion [1–3]. In contrast, far fewer studies have considered the manner in which weak localization is affected under conditions of nonlinear transport. Notable exceptions to this include early works that demonstrated the inability of an electric field to break time-reversal during coherent backscattering [25, 26], and more later experiments on the differential conductance of GaAs/AlGaAs quantum dots [27], short metallic nanobridges [28], and graphene transistors [29, 30]. In spite of these studies, the fact remains that there is still relatively little that is understood about the manner in which weak localization in graphene (as well as in other Dirac materials) is affected under nonequilibrium conditions. It is this specific problem that we address in this paper, in which we derive an expression for the nonlinear differential conductance of weakly-disordered graphene in the presence of weak localization.

In one of the earliest theoretical works to address the role of weak localization, Gor'kov, Larkin, and Khmel'nitskiĭ [31] derived the logarithmic variation of the conductivity that is the hallmark of this phenomenon. Their linear-response calculation revealed a diffusion picture of transport, in which the electron momentum is gradually reversed through a series of elastic-scattering events, thereby accounting for the

*Electronic address: jonas.fransson@physics.uu.se

backscattering that is the source of the localization. This picture was subsequently developed into a comprehensive linear-response theory, in which the localization correction to the classical diffusion current is related to a two-particle propagator known as the Cooperon [2, 3, 32, 33]. The Cooperon consists of a quasiparticle that follows a diffusive path, and which interferes with its time-reversed partner, providing the natural viewpoint from which to discuss weak localization. As a linear-response construct, however, the Cooperon may only be utilized under equilibrium, or quasi-equilibrium, conditions, and hence is not applicable in the nonlinear regime of interest here. We therefore adopt an alternative approach to treat weak localization, as proposed by Shon and Ferraz [34] and also discussed in [35]. The idea is to calculate the charge current flowing through the system under the application of an electric field, by employing nonequilibrium Green functions that allow the (nonequilibrium) distribution of its electronic structure to be accessed. Under spatial averaging, one obtains different classes of diagrams that correspond to distinct physical properties. We specifically distinguish here between rainbow and maximally-crossed diagrams, which provide the impurity-limited average scattering lifetime in the self-consistent Born approximation, and the weak-localization correction, respectively. (Mixed diagrams are omitted since their contributions are generally smaller by an order of magnitude or more, in, for example, the scattering potential.)

As noted above, to calculate the weak-localization correction, and its dependence on voltage bias, we derive an expression for the charge current and the differential conductance of the system, in terms of the nonequilibrium distribution of its electronic structure. With the graphene contacted by a pair of metallic leads, its electronic structure is calculated subject to the boundary conditions imposed by the couplings to these leads. To introduce weak disorder into the graphene layer, we include short-range scattering centers that play the role

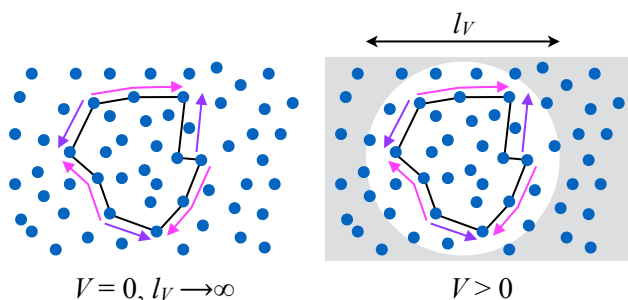


FIG. 1: (Color online) Scattering paths beginning and terminating at the same spatial position in graphene, at zero (left) and non-zero (right) voltage. At zero voltage (and in the absence of any other dephasing mechanisms), the length of the scattering loops is essentially unbounded, generating many contributions to the coherent backscattering responsible for weak localization. At finite bias, the shortened dephasing length due to the applied voltage ultimately limits the length of the scattering loops that contribute to the constructive interference (as indicated by the unshaded area), thereby making weak localization less effective.

of atomically-sharp defects. (The role of long-range disorder, such as that which is typically generated by substrate impurities, is therefore not considered here. In this sense, our analysis is pertinent to intrinsic graphene, in the presence of local imperfections and defects, but free of any substrate interactions.) By performing an impurity average of the electronic structure, we then obtain a description that is local in momentum space, and in which the scattering self-energy can be classified in terms of either rainbow or maximally-crossed diagrams (with mixed diagrams being omitted).

Previously [4], it has been shown that, in order to capture the features of weak localization in graphene, it is necessary to include all Hikami boxes when calculating the Cooperons. In our approach, this amounts to calculating the correction introduced by the maximally-crossed diagrams [34]. In doing so, it is necessary to recognize the importance of the intra- and inter-valley scattering [4], a particular feature of bi-partite lattices such as that in graphene.

Using the methods outlined above, we determine the weak localization correction in graphene, and its dependence on the presence of an applied voltage. The essential outcome of our analytical calculation is that the voltage introduces an additional dephasing time ($\tau_V \sim \hbar/e|V|$) in transport, which in many ways is analogous to the effective dephasing that can also be induced by a magnetic field [2, 36]. If we consider a scenario in which all other sources of dephasing can be neglected, this voltage-induced dephasing represents an unavoidable source of decoherence that places a cut-off on the maximum path length that may be involved in coherent interference (see Fig. 1). In practice, this mechanism will co-exist with other sample-dependent sources of decoherence, including electron-phonon and electron-electron scattering. The voltage-induced dephasing can also be expected to arise in other graphene-like materials, including topological insulators [37, 38] and magnon Dirac materials [39].

The remainder of this paper is organized as follows. In Sec. II, we present our model of weakly-disordered graphene, following which, in Sec. III, we discuss our strategy for the transport calculations. The manner in which impurity scattering is included in the electronic structure is described in Sec. IV, after which our results are discussed and summarized in Sec. V.

II. MODEL OF GRAPHENE WITH A RANDOM DISTRIBUTION OF DEFECTS

Our approach here involves employing a commonly used model for pristine graphene, namely the tight-binding lattice. To account for lattice imperfections, and for other kinds of defects that may be present in graphene, we introduce a random collection of short-ranged impurities into the lattice. Care is necessary in this process, because of the presence of two inequivalent sub-lattices on which the impurities may be located. In our calculations, we will assume that there are equal numbers of impurities in each sub-lattice, since this situation should best correspond to a random-distribution scenario. The role of long-ranged impurities (such as those associated with

some supporting substrate) is not considered in this work, allowing us to identify the intrinsic aspects of weak localization in this material.

We begin by first of all modeling pristine graphene with the following Hamiltonian

$$\mathcal{H}_0 = -t \sum_{\langle ij \rangle \sigma} a_{i\sigma}^\dagger b_{j\sigma} + H.c., \quad (1)$$

where $a_{i\sigma}$ and $b_{j\sigma}$ denote the electron operator in the A- and B- sub-lattice, respectively, the intersite hopping rate is denoted by t , and $\langle ij \rangle$ denotes a summation over nearest neighbors. Under the assumption of a spin-degenerate system, the spin subscript $\sigma = \uparrow, \downarrow$ becomes redundant and is therefore henceforth omitted. Next we add a dilute, random dispersion of impurities through

$$\mathcal{H}_I = \int \Psi^\dagger(\mathbf{r}) \mathbf{V}(\mathbf{r}) \Psi(\mathbf{r}) d\mathbf{r}, \quad (2)$$

where $\Psi(\mathbf{r}) = \int \Psi_{\mathbf{k}} e^{-i\mathbf{k} \cdot \mathbf{r}} d\mathbf{k} / \rho$, ρ is the graphene planar density [44], and

$$\mathbf{V}(\mathbf{r}) = \sum_m \mathbf{V}_m \delta(\mathbf{r} - \mathbf{r}_m) \quad (3)$$

denotes the scattering potential. Here, $\mathbf{V}_m = U \sum_m (\sigma_A \mathbb{1}_{m \in A} + \sigma_B \mathbb{1}_{m \in B})$ with $\sigma_A = (\sigma_0 + \sigma_z)/2$ ($\sigma_B = (\sigma_0 - \sigma_z)/2$), and $\mathbb{1}_{m \in A(B)}$ is the indicator function for \mathbf{r}_m within the A-sublattice (B-sublattice).

In reciprocal space, the model $\mathcal{H}_{\text{gr}} = \mathcal{H}_0 + \mathcal{H}_I$ is transformed into

$$\mathcal{H}_{\text{gr}} = \sum_{\mathbf{k}} \Psi_{\mathbf{k}}^\dagger \Phi_{\mathbf{k}} \Psi_{\mathbf{k}} + \sum_{\mathbf{k}\mathbf{k}'} \Psi_{\mathbf{k}}^\dagger \mathbf{V}_{\mathbf{k}\mathbf{k}'} \Psi_{\mathbf{k}'}. \quad (4)$$

Here

$$\Phi_{\mathbf{k}} = \begin{pmatrix} 0 & \phi_{\mathbf{k}} \\ \phi_{\mathbf{k}}^* & 0 \end{pmatrix}, \quad (5)$$

where the structure factor $\phi_{\mathbf{k}} = -t \sum_j \exp(i\mathbf{k} \cdot \boldsymbol{\delta}_j)$ is given in terms of the nearest neighbor vectors $\boldsymbol{\delta}_1 = a(\sqrt{3}, 1)/2$, $\boldsymbol{\delta}_2 = -a(\sqrt{3}, -1)/2$, and $\boldsymbol{\delta}_3 = -a(0, 1)$, with lattice parameter a . Free electrons have the dispersion relation $\phi_{\mathbf{k} \pm \mathbf{K}} \approx \pm v_F k e^{\pm i\varphi}$ around the K -points $\mathbf{K}_{\pm} = \pm \mathbf{K} = \pm 4\pi \sqrt{3}(1, 0)/9a$, where we have introduced the Fermi velocity $v_F = 3at/2$. Finally, in \mathbf{k} -space the scattering potential assumes the form $\mathbf{V}_{\mathbf{k}\mathbf{k}'} = \sum_m \mathbf{V}_m \exp[-i(\mathbf{k} - \mathbf{k}') \cdot \mathbf{r}_m] / \Omega$, where Ω is the volume of the system.

III. TRANSPORT CALCULATION

In order to compute its conductance, the disordered graphene flake is placed in the junction between a pair of metallic leads, which we model here with Hamiltonians $\mathcal{H}_L = \sum_{\mathbf{p}} (\varepsilon_{\mathbf{p}} - \mu_L) c_{\mathbf{p}}^\dagger c_{\mathbf{p}}$ and $\mathcal{H}_R = \sum_{\mathbf{q}} (\varepsilon_{\mathbf{q}} - \mu_R) c_{\mathbf{q}}^\dagger c_{\mathbf{q}}$, where the chemical potentials $\mu_{L/R}$ are related to the applied voltage V by $\mu_L - \mu_R = eV$. Tunneling between the leads and the graphene

is modeled using $\mathcal{H}_T = \sum_{\mathbf{p}\mathbf{k}} c_{\mathbf{p}}^\dagger t_{\mathbf{p}\mathbf{k}} \Psi_{\mathbf{k}} + \sum_{\mathbf{q}\mathbf{k}} c_{\mathbf{q}}^\dagger t_{\mathbf{q}\mathbf{k}} \Psi_{\mathbf{k}} + H.c.$, where the row vector $t_{\mathbf{p}\mathbf{k}}$ ($t_{\mathbf{q}\mathbf{k}}$) denotes the tunneling rate between the left (right) lead and the graphene, and the pseudo-spinor $\Psi_{\mathbf{k}} = (a_{\mathbf{k}} \ b_{\mathbf{k}})'$. It must be kept in mind that electrons in both sub-lattices take part in tunneling to and from the leads, which is accounted for here by the vectors $t_{\mathbf{p}\mathbf{k}}$ and $t_{\mathbf{q}\mathbf{k}}$.

The stationary charge current flowing between the leads is calculated from $I = -e \partial_t \langle N_L \rangle = -e \partial_t \sum_{\mathbf{k}\sigma} \langle c_{\mathbf{p}\sigma}^\dagger c_{\mathbf{p}\sigma} \rangle$. Using standard methods we write this current as

$$I = \frac{ie}{h} \text{tr} \sum_{\mathbf{k}\mathbf{k}'} \int \Gamma^L(\mathbf{k}, \mathbf{k}') \left(f_L(\omega) \mathbf{G}^>(\mathbf{k}', \mathbf{k}; \omega) + f_L(-\omega) \mathbf{G}^<(\mathbf{k}', \mathbf{k}; \omega) \right) d\omega, \quad (6)$$

where the trace runs over the pseudo-spin degrees of freedom, and $f_{\chi}(x) = f(\omega - \mu_{\chi})$ is the Fermi function at the chemical potential μ_{χ} . Here, $\Gamma^{\chi}(\mathbf{k}, \mathbf{k}')$ denotes the coupling between the lead $\chi = L, R$ and the central region. In what follows, we omit the momentum dependence of the coupling, such that $\Gamma^{\chi}(\mathbf{k}, \mathbf{k}') = \Gamma^{\chi}$. We moreover assume that the lesser/greater Green function for the central region $\mathbf{G}^{</>}(\mathbf{k}, \mathbf{k}'; \omega)$ has a simple momentum dependence, that is, $\mathbf{G}^{</>}(\mathbf{k}, \mathbf{k}') = \mathbf{G}_{\mathbf{k}}^{</>}$. While these restrictions may appear arbitrary, it will become clear in later sections that they arise rather naturally in these forms under the circumstances that we study. Below we will consider the differential conductance dI/dV , but we leave the details of the calculation of this quantity until later.

From the expression for the charge current, Eq. (6), it can be seen that the essential physics that we aim to describe is contained in the lesser and greater Green functions. The task in the following sections is to provide a coherent picture of the transport properties in terms of these correlation functions.

IV. ELECTRONIC STRUCTURE CALCULATION

In this section, we discuss how we use Green function techniques to calculate the electronic structure properties, and thus the weak localization correction, in graphene. Since we assume nonequilibrium conditions, we have to expand on the Keldysh contour and nonequilibrium Green functions. Absence of time-dependent fields and processes allows for a conversion to Fourier space, keeping in mind that the propagators are functions of the complex variable z and that physical quantities are obtained through analytical continuation.

The electronic structure of pristine graphene is described by the *free* (unperturbed) graphene Green function

$$\mathbf{g}(\mathbf{k}; z) = \frac{1}{z^2 - |\phi_{\mathbf{k}}|^2} \begin{pmatrix} z & \phi_{\mathbf{k}} \\ \phi_{\mathbf{k}}^* & z \end{pmatrix}. \quad (7)$$

With these prerequisites, we can write the equation of motion for the Green function $\mathbf{G}(\mathbf{k}, \mathbf{k}'; z) = \langle \langle \Psi_{\mathbf{k}} | \Psi_{\mathbf{k}'}^\dagger \rangle \rangle(z)$ as the Dyson equation

$$\mathbf{G}(\mathbf{k}, \mathbf{k}') = \delta_{\mathbf{k}\mathbf{k}'} \mathbf{g}_{\mathbf{k}} + \sum_{\mathbf{k}''} \mathbf{g}_{\mathbf{k}} \mathbf{V}_{\mathbf{k}\mathbf{k}''} \mathbf{G}(\mathbf{k}'', \mathbf{k}'). \quad (8)$$

The equation of motion can be expanded in orders of the scattering potential $\mathbf{V}_{\mathbf{k}\mathbf{k}'}$, according to

$$\mathbf{G}(\mathbf{k}, \mathbf{k}') = \delta_{\mathbf{k}\mathbf{k}'} \mathbf{g}_{\mathbf{k}} + \mathbf{g}_{\mathbf{k}} \mathbf{V}_{\mathbf{k}\mathbf{k}'} \mathbf{g}_{\mathbf{k}'} + \sum_{\kappa} \mathbf{g}_{\mathbf{k}} \mathbf{V}_{\mathbf{k}\kappa} \mathbf{g}_{\kappa} \mathbf{V}_{\kappa\mathbf{k}'} \mathbf{g}_{\mathbf{k}'} + \dots \quad (9)$$

which enables an order-by-order investigation of the electronic structure. Due to the random distribution of impurities, and rather than resorting to numerical simulations, we can make analytical progress here by performing impurity averaging of each contribution in the above expansion.

Before proceeding, we also note that expansion of the Green function in Eq. (9) leads to a corresponding expansion of the current, allowing it to be expressed in the form $I = I_0 + \delta I$. The leading term here contains impurity scattering to the level of the self-consistent Born approximation, in which scattering from different impurities is taken to be independent, and so only provides a lifetime broadening in the density of electron states. It is the correction δI , on the other hand, that pertains to weak localization, and in the remainder of this article we therefore focus on determining this term, without paying any further attention to I_0 .

Due to the expansion in Eq. (9), and to the impurity averaging, the decomposition of the current can be viewed as an effect of the lesser/greater Green function, which can be written as

$$\mathbf{G}^{</>}(\mathbf{k}) = \overline{\mathbf{G}}^r(\mathbf{k}) (\Sigma_0^{</>} + \Sigma_{cr}^{</>}(\mathbf{k})) \overline{\mathbf{G}}^a(\mathbf{k}). \quad (10)$$

Here, the retarded/advanced Green function $\overline{\mathbf{G}}^{r/a}(\mathbf{k})$ includes scattering up to the level of the self-consistent Born approximation. The self-energy $\Sigma_0^{</>}$ accounts for the coupling to the leads, and hence the nonequilibrium nature of the problem, and describes impurity scattering up to the level necessary to capture weak localization. As we shall see below, $\Sigma_0^{</>}$ is included in $\Sigma_{cr}^{</>}$ also, allowing us to write $\Sigma_{cr}^{</>} = \Sigma_0^{</>} \mathbf{Z}$ where \mathbf{Z} is a matrix comprising the impurity scattering not included in $\Sigma_0^{</>}$. This naturally leads to the decomposition of the current in terms of its regular component I_0 and a correction δI attributed to weak localization.

A. Impurity averaging

To calculate the weak localization correction to the conductance, we make an average over impurities located at positions $\{\mathbf{r}_m\}$, thereby accounting for their presence in a mean-field form that surrenders the non-locality of the Green function in reciprocal space. To first order in the scattering potential, we obtain

$$\begin{aligned} \overline{\mathbf{V}}_{\mathbf{k}\mathbf{k}'} &\equiv \langle \mathbf{V}_{\mathbf{k}\mathbf{k}'}(\{\mathbf{r}_\alpha\}) \rangle_{\text{imp}} = \prod_{\alpha} \int \mathbf{V}_{\mathbf{k}\mathbf{k}'}(\{\mathbf{r}_\alpha\}) \frac{d\mathbf{r}_\alpha}{\Omega} \\ &= \prod_{\alpha} \int \frac{1}{\Omega} \sum_m \mathbf{V}_m e^{-i(\mathbf{k}-\mathbf{k}') \cdot \mathbf{r}_m} \frac{d\mathbf{r}_\alpha}{\Omega} \\ &= \frac{1}{\Omega} \sum_m \mathbf{V}_m \delta_{\mathbf{k}\mathbf{k}'} = \frac{U}{\Omega} (N_A \sigma_A + N_B \sigma_B) \delta_{\mathbf{k}\mathbf{k}'}. \end{aligned} \quad (11)$$

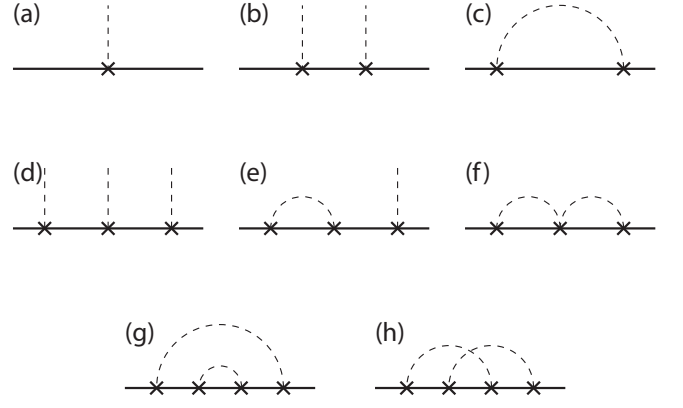


FIG. 2: Some of the low-order diagrams that are important for conductivity calculations. Momentum is conserved at each vertex. Solid (dashed) lines represent free-electron Green function (impurity potential), whereas crosses mark scattering events. Diagrams (c), (f), and (g) are the lowest-order rainbow diagrams, whereas diagram (h) is the lowest-order crossed diagram.

The Feynman diagram corresponding to this first-order scattering process is depicted in Fig. 2(a). Under the assumption of equal numbers of impurities in the two sublattices, $N_A = N_B = N$, we can write

$$\overline{\mathbf{V}}_{\mathbf{k}\mathbf{k}'} = \frac{N}{\Omega} V \sigma_0 \delta_{\mathbf{k}\mathbf{k}'} = c U \sigma_0 \delta_{\mathbf{k}\mathbf{k}'}, \quad (12)$$

where $c = N/\Omega$ defines the concentration of impurities. This leads to the result that the first-order correction to the reciprocal space Green function is given by

$$\delta \mathbf{G}_{\mathbf{k}}^{(1)} = c U \mathbf{g}_{\mathbf{k}}^2. \quad (13)$$

Applying the same procedure to the second-order component in Eq. (9), we obtain

$$\begin{aligned} \overline{\mathbf{V}_{\mathbf{k}\kappa} \mathbf{g}_{\kappa} \mathbf{V}_{\kappa\mathbf{k}'}} &= \frac{1}{\Omega^2} \left(\sum_{m \neq n} \mathbf{V}_m \mathbf{g}_{\kappa} \mathbf{V}_n \delta_{\mathbf{k}\mathbf{k}'} + \sum_m \mathbf{V}_m \mathbf{g}_{\kappa} \mathbf{V}_m \right) \delta_{\mathbf{k}\mathbf{k}'} \\ &= \frac{N U^2}{\Omega^2} \left((N-1) \mathbf{g}_{\kappa} \sigma_0 + \sum_{i=A,B} \sigma_i \mathbf{g}_{\kappa} \sigma_i \right) \delta_{\mathbf{k}\mathbf{k}'}. \end{aligned} \quad (14)$$

The Feynman diagrams corresponding to this second-order scattering process are depicted in Figs. 2(b) and 2(c), respectively. We notice here that the distribution of impurities between the two sub-lattices leads to a restricted contribution from $\sum_{\kappa} \mathbf{g}_{\kappa}$, such that it picks out just the diagonal components. While this structural organization is unimportant for the second-order contribution, we shall see below that it can be extremely important for some of the higher-order ones.

The second-order correction can be summarized as

$$\delta \mathbf{G}_{\mathbf{k}}^{(2)} = c^2 U^2 \left[1 - \frac{1}{N} \right] \mathbf{g}_{\mathbf{k}}^3 + c U^2 \mathbf{g}_{\mathbf{k}} \tilde{\mathbf{g}} \mathbf{g}_{\mathbf{k}}, \quad (15)$$

where $\tilde{\mathbf{g}} = \sum_{i=A,B} \sum_{\kappa} \sigma_i \mathbf{g}_{\kappa} \sigma_i$. Here, again, the first term is structureless and so unimportant to our discussion, since it can

be absorbed into the single-particle energy. The last term, on the other hand, is of major interest since it provides the first diagram in the class of rainbow diagrams, see Fig. 2(c). A partial summation over this class of diagrams leads to a dressed graphene Green function and, hence, to the electronic structure in which the effective impurity limited scattering life-time τ_I is included. Taking this observation as guidance, we define the self-energy in the self-consistent Born approximation in terms of the impurity averaged Green function $\bar{\mathbf{G}}$ (where $u^2 = cU^2$)

$$\Sigma = \frac{u^2}{\Omega} \sum_{i=A,B} \sum_{\mathbf{k}} \sigma_i \bar{\mathbf{G}}_{\mathbf{k}} \sigma_i, \quad (16)$$

where the impurity averaged Green function is given in terms of the Dyson equation $\bar{\mathbf{G}}(\mathbf{k}) = (\mathbf{g}^{-1}(\mathbf{k}) - \Sigma[\bar{\mathbf{G}}])^{-1}$. By making the ansatz $\Sigma^r(\omega) = (\Lambda - i/2\tau_I)\sigma_0$ for the retarded form of the self-energy, we can evaluate this energy as

$$\begin{aligned} & \frac{u^2}{\Omega} \sum_{i=A,B} \sum_{\mathbf{k}} \sigma_i \bar{\mathbf{G}}_{\mathbf{k}}^r \sigma_i \\ &= -\frac{4u^2}{D_c^2} \left(\omega + \frac{i}{2\tau_I} \right) \left(\ln \frac{D_c}{|\omega + i/2\tau_I|} + i\frac{\pi}{2} \text{sign}(\omega) \right) \sigma_0, \end{aligned} \quad (17)$$

where $D_c^2 = 4\pi v_F^2$ defines an upper energy cut. Equating for Λ and $1/\tau_I$ we find that

$$\Lambda = 4\omega \frac{u^2}{D_c^2} \left(\pi^2 \frac{u^2}{D_c^2} - \ln \frac{D_c}{|\omega + i/2\tau_I|} + 4 \frac{u^2}{D_c^2} \ln^2 \frac{D_c}{|\omega + i/2\tau_I|} \right), \quad (18a)$$

$$\frac{1}{\tau_I} = 4\pi|\omega| \frac{u^2/D_c^2}{1 - 4(u^2/D_c^2) \ln(D_c/|\omega + i/2\tau_I|)}. \quad (18b)$$

These results are valid as long as $1/\tau_I \ll 1$, which is sufficient for small energies around the Fermi level since $D_c \sim 1$ eV while $u^2|\omega|/D_c^2 \ll 10^{-3}$, implying that $4(u^2/D_c^2) \ln(D_c/|\omega + i/2\tau_I|) \ll 1$. We may therefore neglect Λ , and retain only the approximate inverse life-time

$$\frac{1}{\tau_I} \approx \frac{4\pi u^2}{D_c^2} |\omega|. \quad (19)$$

Summation over all diagrams of this (self-consistent Born approximation) type describes the essential non-zero temperature transport for the materials that we consider. For instance, in the case of two-dimensional metals this leads to the usual Ohmic current-voltage dependence, whereas the scattering processes which involve a higher degree of correlations between the Feynman paths give only a negligible contribution. In the low-temperature regime this statement is not valid any longer as we shall see in the subsequent discussion.

In the high-temperature range, one can essentially argue from assumptions [35] that, since all relevant momenta and energies are confined to the neighborhood of the Fermi surface, any difference in magnitude between higher-order diagrams of type (g) and (h) in Fig. 2 must lie in the angular integrations. For diagrams of type (g), each of the three Green

functions yields a contribution of $1/\tau_I$ where τ_I is the elastic scattering life-time, which leads to an overall contribution of order $(cU^2)^2 \tau_I^{-3}$. For diagrams of type (h), on the other hand, only two Green functions contribute to τ_I^{-1} and angular integration of the third leads to a contribution of the order of ε_F^{-1} , where ε_F is the Fermi energy. The ratio between these two types of diagrams is therefore of order $1/\varepsilon_F \tau_I \propto 1/k_F l \ll 1$, where k_F is the Fermi momentum and $l = v_F \tau_I$ is the impurity mean free path (with v_F the Fermi velocity). While this line of argument applies well to conventional metals, the situation is somewhat more subtle for graphene. Nonetheless, at sufficiently high temperatures, the above arguments are satisfactory.

B. Maximally-crossed diagrams

In the theory of weak localization for weakly-disordered metals, it is well known that diagrams containing crossed impurity lines are smaller by a factor $(lk_F)^{-1}$ than those (of the same order in the impurity potential) without any such lines [35]. On the other hand, the maximally-crossed diagrams give rise to a contribution that is of the same order of magnitude as that generated by the uncrossed ones. Hence, in constructing the self-energy functional for the kinetic equation, it is necessary to sum over the maximally-crossed diagrams.

An example of a maximally-crossed diagram is shown in Fig. 2(h), which represents the lowest order diagram in this class. Algebraically, this diagram can be written as

$$\begin{aligned} \Sigma_{cr}^{(1)}(\mathbf{k}) &= \frac{1}{\Omega^4} \sum_{m \neq n} \sum_{\mathbf{q}\mathbf{\kappa}} \mathbf{V}_m \bar{\mathbf{G}}_{\mathbf{p}/2+\mathbf{\kappa}} \mathbf{V}_n \bar{\mathbf{G}}_{\mathbf{q}} \mathbf{V}_m \bar{\mathbf{G}}_{\mathbf{p}/2-\mathbf{\kappa}} \mathbf{V}_n \\ &\approx \frac{u^4}{\Omega^2} \sum_{\mathbf{q}\mathbf{\kappa}} \sum_{i,j=A,B} \sigma_i \bar{\mathbf{G}}_{\mathbf{p}/2+\mathbf{\kappa}} \sigma_j \bar{\mathbf{G}}_{\mathbf{q}} \sigma_i \bar{\mathbf{G}}_{\mathbf{p}/2-\mathbf{\kappa}} \sigma_j, \end{aligned} \quad (20)$$

where $\mathbf{p} = \mathbf{k} + \mathbf{q}$, again under the assumption that the number of impurities $N \gg 1$. An alternative way to represent the diagram corresponding to this lowest order maximally-crossed diagram is given in Fig. 3, which further illustrates the convoluted character of the propagation (lines) between the scattering centers (crosses). The dominant contribution to the lesser/greater form of the self-energy is then given by [35]

$$\Sigma_{cr}^{(1)</>}(\mathbf{k}) = \frac{u^4}{\Omega^2} \sum_{\mathbf{q}\mathbf{\kappa}} \sum_{i,j=A,B} \sigma_i \bar{\mathbf{G}}_{\mathbf{p}/2+\mathbf{\kappa}}^r \sigma_j \bar{\mathbf{G}}_{\mathbf{q}}^{</>} \sigma_i \bar{\mathbf{G}}_{\mathbf{p}/2-\mathbf{\kappa}}^a \sigma_j. \quad (21)$$

Before we continue with the evaluation of this diagram, we make a few observations concerning the matrices σ_A and σ_B . First, these matrices are projections, such that $\sigma_i^2 = \sigma_i$, and they are clearly orthogonal ($\sigma_A \sigma_B = 0 = \sigma_B \sigma_A$). Moreover, for a general 2×2 matrix \mathbf{A} , we have $\sigma_A \mathbf{A} \sigma_A = A_{11} \sigma_A$ and $\sigma_B \mathbf{A} \sigma_B = A_{22} \sigma_B$, while $\sigma_A \mathbf{A} \sigma_B = A_{12} \sigma_+$ and $\sigma_B \mathbf{A} \sigma_A = A_{21} \sigma_-$, where $\sigma_{\pm} = (\sigma_x \pm i\sigma_y)/2$. Hence, any matrix product

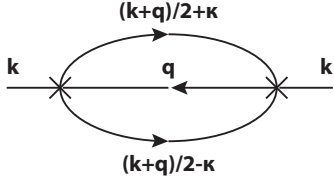


FIG. 3: Feynman diagram corresponding to the self-energy in Eq. (20), where electron propagation is denoted by lines and scattering by crosses.

on the form $\sigma_i \mathbf{A} \sigma_j \mathbf{B} \sigma_i \mathbf{C} \sigma_j$ can be reduced to

$$\sum_{i,j=A,B} \sigma_i \mathbf{A} \sigma_j \mathbf{B} \sigma_i \mathbf{C} \sigma_j = \sum_{i,j=A,B} (\sigma_i \mathbf{A} \sigma_j) (\sigma_j \mathbf{B} \sigma_i) (\sigma_i \mathbf{C} \sigma_j) = \begin{pmatrix} A_{11} B_{11} C_{11} & A_{12} B_{21} C_{12} \\ A_{21} B_{12} C_{21} & A_{22} B_{22} C_{22} \end{pmatrix}. \quad (22)$$

Due to this latter property of the matrix structure, we can perform all evaluations of the crossed diagrams element by element. While these calculations are somewhat straightforward, we briefly go through some of their important features here.

Firstly, working under our assumption of spin-degeneracy, the diagonal components of the graphene Green function are equal and we, therefore, only have to consider one of them. An analogous observation holds for the off-diagonal components. Secondly, calculation of all matrix components in the self-energy is fundamentally important since the coupling between the pseudo-spin degrees of freedom plays a central role in the theory of weak localization in graphene [4]. Making use of these properties, along with those of the crossed diagrams summarized in Eq. (22), we write the upper left and right components to $\Sigma_{cr}^{(1)</>}(\mathbf{k})$ as

$$(\Sigma_{cr}^{(1)</>}(\mathbf{k}))_{11} = \frac{u^2}{\Omega} \sum_{\mathbf{q}} \zeta_{11}(\mathbf{p}) (\bar{\mathbf{G}}_{\mathbf{q}}^{</>})_{11}, \quad (23a)$$

$$(\Sigma_{cr}^{(1)</>}(\mathbf{k}))_{12} = \frac{u^2}{\Omega} \sum_{\mathbf{q}} \zeta_{12}(\mathbf{p}) (\bar{\mathbf{G}}_{\mathbf{q}}^{</>})_{21}, \quad (23b)$$

where the subscripts refer to matrix components and where

$$\zeta_{11}(\mathbf{p}) = \frac{u^2}{\Omega} \sum_{\kappa} (\bar{\mathbf{G}}_{\mathbf{p}/2+\kappa}^r)_{11} (\bar{\mathbf{G}}_{\mathbf{p}/2-\kappa}^a)_{11}, \quad (24a)$$

$$\zeta_{12}(\mathbf{p}) = \frac{u^2}{\Omega} \sum_{\kappa} (\bar{\mathbf{G}}_{\mathbf{p}/2+\kappa}^r)_{12} (\bar{\mathbf{G}}_{\mathbf{p}/2-\kappa}^a)_{12}. \quad (24b)$$

To evaluate the momentum summation contained in the expression for ζ_{ij} , we expand the Green functions around the nodes in the two valleys $\pm \mathbf{K}$. The influence of both intra- and inter-valley scattering, necessary to the theoretical description of weak localization [4], is included in this problem by individually expanding the Green functions in the two valleys, in the product above. While this individual expansion is unimportant for the diagonal components, it is crucial for the off-

diagonal ones. Hence, expanding around $\pm \mathbf{K}$ leads to

$$\phi_{\mathbf{p}/2 \pm \kappa + \mathbf{K}} \approx \frac{v_F}{2} (p e^{i\varphi_{\mathbf{p}}} \pm 2\kappa e^{i\varphi_{\kappa}}), \quad (25a)$$

$$\phi_{\mathbf{p}/2 \pm \kappa - \mathbf{K}} \approx -\frac{v_F}{2} (p e^{-i\varphi_{\mathbf{p}}} \pm 2\kappa e^{-i\varphi_{\kappa}}), \quad (25b)$$

where $\tan \varphi_{\mathbf{K}} = k_y/k_x$ and $\tan \varphi_{\mathbf{p}} = p_y/p_x$. Expanding the product of the structure factors in the two valleys then gives

$$\phi_{\mathbf{p}/2+\kappa} \phi_{\mathbf{p}/2-\kappa} \approx -E^2 \sin^2 \varphi_{\mathbf{p}} + 4\varepsilon^2 \sin^2 \varphi_{\kappa}, \quad (26)$$

where $E = v_F p$ and $\varepsilon = v_F \kappa$. Moreover, since $|\phi_{\mathbf{p}/2 \pm \kappa}| \rightarrow v_F |\mathbf{p}/2 \pm \kappa|$ in the valleys, and restricting ourselves to the regime $E \ll \varepsilon_F$, we can employ the approximation $v_F^2 |\mathbf{p}/2 \pm \kappa|^2 \approx \varepsilon^2 \pm \varepsilon_F E \cos \gamma$. Then, by introducing the notation $(z_{\mp}^{r/a})^2 = (z^r/a)^2 \mp \varepsilon_F E \cos \gamma$, with $z^r/a = \omega \pm i/2\tau$ and $\gamma = \varphi_{\kappa} - \varphi_{\mathbf{p}}$, we can write

$$\zeta_{11}(\mathbf{p}) = \frac{8u^2}{D_c^2} \int \frac{|z^r|^2}{[(z_-^r)^2 - \varepsilon^2][(z_+^a)^2 - \varepsilon^2]} \frac{\varepsilon d\varepsilon d\varphi_{\kappa}}{2\pi}, \quad (27a)$$

$$\zeta_{12}(\mathbf{p}) = -\frac{2u^2}{D_c^2} \int \frac{E^2 \sin^2 \varphi_{\mathbf{p}} - 4\varepsilon^2 \sin^2 \varphi_{\kappa}}{[(z_-^r)^2 - \varepsilon^2][(z_+^a)^2 - \varepsilon^2]} \frac{\varepsilon d\varepsilon d\varphi_{\kappa}}{2\pi}. \quad (27b)$$

In these expressions, the energy (ε) integral generates the logarithm

$$\log \frac{D_c^2}{-(z_-^r)^2} \frac{-(z_+^a)^2}{D_c^2} \approx i2\pi, \quad (28)$$

and a logarithmic dependence similarly appears in the integration in ζ_{12}

$$\log \frac{D_c^4}{(z_-^r)^2 (z_+^a)^2} \approx 4 \ln \frac{D_c}{|\omega|}. \quad (29)$$

In these equations, we have omitted any angular dependence from the logarithms. In the latter case, the denominator $(z_-^r)^2 (z_+^a)^2$ then becomes proportional to ω^4 , resulting in the final form shown on the right-hand side of this equation. We should also mention at this stage that the logarithmic energy dependence that arises in ζ_{12} crucially influences the differential conductance. As we will see shortly, this dependence is manifested directly in the transport properties of the material.

We can now write the kernels ζ_{ij} according to

$$\zeta_{11}(\mathbf{p}) = i \frac{2\pi u^2}{D_c^2} \int \frac{|z^r|^2}{i\omega/\tau - \varepsilon_F E \cos \gamma} \frac{d\varphi_{\kappa}}{2\pi}, \quad (30a)$$

$$\zeta_{12}(\mathbf{p}) = -\frac{u^2}{D_c^2} \int \left(4 \sin^2 \varphi_{\kappa} \ln \frac{D_c}{|\omega|} - i\pi \frac{E^2 \sin^2 \varphi_{\mathbf{p}} - 4\omega^2 \sin^2 \varphi_{\kappa}}{i\omega/\tau - \varepsilon_F E \cos \gamma} \right) \frac{d\varphi_{\kappa}}{2\pi}. \quad (30b)$$

Then, by finally performing the angular integration, we arrive at the expressions

$$\zeta_{11}(\mathbf{p}) = \frac{2\pi u^2}{D_c^2} \frac{\omega^2}{\sqrt{(\omega/\tau)^2 + (\varepsilon_F E)^2}}, \quad (31a)$$

$$\zeta_{12}(\mathbf{p}) = -\frac{u^2}{D_c^2} \left(2 \ln \frac{D_c}{|\omega|} - \pi \frac{E^2 - 4\omega^2}{\sqrt{(\omega/\tau)^2 + (\varepsilon_F E)^2}} \sin^2 \varphi_{\mathbf{p}} \right), \quad (31b)$$

where in the result for ζ_{11} we have replaced $|z'|$ by ω (since $1/4\tau^2 \ll \omega^2$) and in that for ζ_{12} we have neglected a minor contribution proportional to ω^2 . In fact, the second contribution to ζ_{12} can also be omitted since it merely renormalizes the final expression without changing its vital properties pertaining to weak localization.

Our calculation of the maximally crossed diagrams, in the first order of the self-energy, yields the expression

$$\Sigma_{cr}^{(1)</>}(\mathbf{k}) = \frac{u^2}{\Omega} \sum_{\mathbf{q}} \left\{ \frac{2\pi u^2 \omega^2 / D_c^2}{\sqrt{(\omega/\tau)^2 + (\varepsilon_F E)^2}} \begin{pmatrix} (\bar{\mathbf{G}}_{\mathbf{q}}^{</>})_{11} & 0 \\ 0 & (\bar{\mathbf{G}}_{\mathbf{q}}^{</>})_{22} \end{pmatrix} - \frac{2u^2}{D_c^2} \ln \frac{D_c}{|\omega|} \begin{pmatrix} 0 & (\bar{\mathbf{G}}_{\mathbf{q}}^{</>})_{21} \\ (\bar{\mathbf{G}}_{\mathbf{q}}^{</>})_{12} & 0 \end{pmatrix} \right\}. \quad (32)$$

The real power of the matrix structure of Eq. (22) is now seen when we sum up over the higher-order contributions to the maximally-crossed diagrams, since the n th contribution to both the diagonal and off-diagonal terms in this summation is simply equal to the n th power of the entries in the expression above. Hence, the summation over the maximally-crossed diagrams can be performed as four separate geometric series, such that

$$\sum_{n=1}^{\infty} (\zeta_{11}(\mathbf{p}))^n = \sum_{n=1}^{\infty} (\zeta_{22}(\mathbf{p}))^n \approx \frac{(\omega/\tau\varepsilon_F)^2}{E^2 + (\omega/\tau\varepsilon_F)^2}, \quad (33a)$$

$$\sum_{n=1}^{\infty} (\zeta_{12}(\mathbf{p}))^n = \sum_{n=1}^{\infty} (\zeta_{21}(\mathbf{p}))^n \approx -\frac{2u^2}{D_c^2} \ln \frac{D_c}{|\omega|}. \quad (33b)$$

In the expression for ζ_{11} (ζ_{22}), we have made use of the relation $4\pi u^2 / D_c^2 \approx 1/\tau|\omega|$. The self-energy contribution from the maximally-crossed diagrams is then reduced to the expression

$$\Sigma_{cr}^{</>}(\mathbf{k}) = \frac{u^2}{\Omega} \sum_{\mathbf{q}} \left\{ \frac{(\omega/\tau\varepsilon_F)^2}{E^2 + (\omega/\tau\varepsilon_F)^2} \begin{pmatrix} (\bar{\mathbf{G}}_{\mathbf{q}}^{</>})_{11} & 0 \\ 0 & (\bar{\mathbf{G}}_{\mathbf{q}}^{</>})_{22} \end{pmatrix} - \frac{2u^2}{D_c^2} \ln \frac{D_c}{|\omega|} \begin{pmatrix} 0 & (\bar{\mathbf{G}}_{\mathbf{q}}^{</>})_{21} \\ (\bar{\mathbf{G}}_{\mathbf{q}}^{</>})_{12} & 0 \end{pmatrix} \right\}. \quad (34)$$

Next, we sum over the momentum \mathbf{q} . In the diagonal components, we note that $1/[E^2 + (\tau\varepsilon_F/\omega)^2]$ is strongly peaked around $\mathbf{q} = -\mathbf{k}$, and recall that $E = v_F|\mathbf{k} + \mathbf{q}|$, which allows us to move $(\bar{\mathbf{G}}_{\mathbf{q}}^{</>})_{11(22)}$ out of the summation, the remainder of which yields the factor

$$\left(\frac{u}{D_c} \right)^2 \left(\frac{\omega}{\tau\varepsilon_F} \right)^2 \log \left[1 + \left(\frac{\tau\varepsilon_F D_c}{\omega} \right)^2 \right] \approx \left(\frac{u}{D_c} \right)^2 \left(\frac{\omega}{\tau\varepsilon_F} \right)^2 \left(\frac{\tau\varepsilon_F D_c}{\omega} \right)^2 = u^2 \ll 1. \quad (35)$$

Continuing with the summation of the off-diagonal components, this can be performed over $(\bar{\mathbf{G}}_{\mathbf{q}}^{</>})_{12(21)}$ since the contribution from ζ_{12} is independent of \mathbf{q} . Here, we set $\bar{\mathbf{G}}_{\mathbf{q}}^{</>} = \bar{\mathbf{G}}_{\mathbf{q}}^r \Sigma_0^{</>} \bar{\mathbf{G}}_{\mathbf{q}}^a$, where $\Sigma_0^{</>}(\omega) = (\pm i) \sum_{\chi} \Gamma_{\chi} f_{\chi}(\pm\omega)(\sigma_0 + \sigma_{\chi})$ is

the self-energy due to the coupling to the two leads. These considerations lead to

$$\Sigma_{cr}^{</>}(\mathbf{k}) \approx (\pm i) \sum_{\chi} \Gamma_{\chi} f_{\chi}(\pm\omega) \left[\sigma_0 u^2 \left| (\bar{\mathbf{G}}_{-\mathbf{k}}^r)_{11} + (\bar{\mathbf{G}}_{-\mathbf{k}}^r)_{12} \right|^2 - \sigma_{\chi} \frac{3u^2}{D_c^2} \ln \frac{D_c}{|\omega|} \right]. \quad (36)$$

The diagonal components in this expression provide a contribution to the current that is quartic in the Green functions, which should be compared with the quadratic contribution generated by the off-diagonal terms. Since the multiplying factor is also constant, when compared to the logarithmic functions in the off-diagonal components, the diagonal components can be discarded when calculating the weak-localization correction. It is interesting to note that this correction appears in the off-diagonal components of the self-energy, and, hence, of the Green function. These components account for the coupling between electrons in different sublattices, indicating that the pseudo-spin chirality is of great importance for the emergence of weak localization in graphene. The imaginary part of the self-energy can be associated with a dephasing time $1/\tau_V \sim (u/D_c)^2 \ln D_c/|\omega|$, which, in this order of approximation, diverges as $\omega \rightarrow 0$. In the differential conductance, as we will see shortly below, the energy (ω) dependence is replaced by a dependence on voltage.

From this point, calculation of the (differential) conductance dI/dV essentially reduces to taking the derivative of the Fermi functions. Recalling that the conductance is given by the product of the trace of the coupling matrix and the lesser/greater Green functions, see Eq. (6), we obtain the energy-dependent conductance correction

$$\frac{d\delta I}{dV} = -\frac{2e^2}{h} \Gamma^L \Gamma^R \int \mathcal{F}_V(\omega) \frac{1}{D_c^2} \ln \frac{D_c}{|\omega|} d\omega, \quad (37)$$

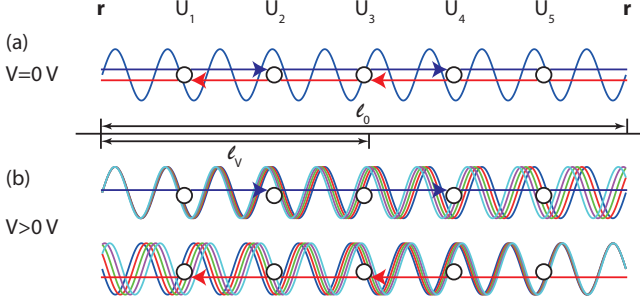
which displays the logarithmic dependence normally associated with weak localization (in linear transport). Here, $\mathcal{F}_V(\omega) = (\beta/4) \cosh^{-2} \beta(\omega - eV)/2 \rightarrow \delta(\omega - eV)$, $T \rightarrow 0$. The correction in Eq. (37) should be compared to the bare conductance

$$\frac{dI_0}{dV} = \frac{2e^2}{h} \Gamma^L \Gamma^R \frac{4}{u^2}, \quad (38)$$

in which the presence of the scattering potential ($u^2 = cV^2$) corresponds, in the self-consistent Born approximation, to the Drude resistance of the material in the presence of impurity scattering. The quantum correction accounted for in $d\delta I/dV$, on the other hand, describes the suppression of weak localization as the voltage is increased from zero, resulting in a logarithmic increase of the conductance [45].

V. DISCUSSIONS AND SUMMARY

One of the key findings of our study is the derivation of an energy-dependent dephasing time (Eq. (19)), which accounts



for the suppression of weak localization under nonequilibrium conditions. In the situation considered here, this suppression arises from the application of a non-zero voltage, allowing us to define a corresponding dephasing time $\tau_v \sim (D_c/u)^2 / \ln(D_c/|V|)$. This *voltage-induced* dephasing time has no corresponding analog in conventional 2D materials (with quadratic energy dispersion and an energy-independent density states), but arises instead from the pseudo-spin chirality of graphene. Formally, the dephasing is introduced into the scattering self-energy due to the influence of the maximally-crossed diagrams in Eq. (29). Referring to Fig. 4, we associate the voltage-induced dephasing with the phase evolution that develops among diffusing wavepackets, when they possess a spread of energies arising from an applied voltage. At zero bias, the coherent-backscattering process involves the interference of monoenergetic waves that traverse closed loops in opposite directions, and the coherence length is essentially set by electron-electron and electron-phonon scattering. At non-zero bias, however, diffusing electrons are represented by a set of waves, with a spread of energies determined by the value of the applied voltage. This spread leads to a natural decoherence, and to a corresponding reduction in the magnitude of the weak-localization correction.

The energy-dependent lifetime derived in Eq. (19) is a consequence of the linear energy dispersion of graphene, but is not unique to this material; it has also been obtained in studies of topological insulators [37, 38], and in magnon Dirac materials [39]. A similarly energy-dependent lifetime has moreover been found in experimental and theoretical studies of the influence of individual and multiple scattering centers in graphene [46–48], in which systems the width of the impurity resonance typically decreases the closer the resonance is to

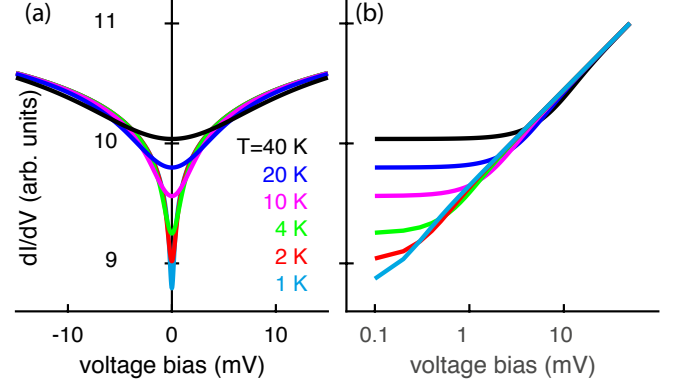


FIG. 5: (Color online) Differential conductance as a function of voltage, plotted on (a) linear and (b) logarithmic scales. The calculations were performed for the following parameters: $D_c = 3$ eV, (scattering potential) $U \sim 10$ eV, and (impurity concentration) $c = 1\%$.

the Dirac point. The same property, namely the energy dependence of the impurity resonance width, is retained also in the presence of impurity averaging, as would be expected from the self-consistent Born approximation.

In Fig. 5(a), we show the calculated differential conductance due to weak localization at several different temperatures. These plots were calculated by numerically differentiating the current, determined from Eq. (6) using the nonequilibrium distribution functions ($G^{</>}(\mathbf{k})$) derived in Sec. IV. The weak localization is responsible for the suppression of the differential conductance near zero bias. Reflecting the thermal broadening introduced by the Fermi functions, the strength of this suppression grows steadily as the temperature is lowered. Qualitatively, at least, these behaviors resemble those reported in recent experiments [29, 41, 49]. In Fig. 5(b), we re-plot the differential-conductance data of panel (a) with voltage indicated on a logarithmic axis, revealing the presence of a temperature-dependent threshold beyond which the conductance increases logarithmically with voltage. A careful inspection of these data shows that the crossover from an invariant to a logarithmically increasing conductance occurs once the size of the energy window (eV) opened by the applied voltage exceeds the thermal energy ($k_B T$). This should provide a quantitative prediction for comparison with future experiment.

In summary, in this theoretical study we have explored the manner in which the quantum correction due to weak localization is suppressed in weakly-disordered graphene under the application of a nonequilibrium voltage. Our calculations of the charge current and the resulting differential conductance reveal the typical logarithmically-divergent behavior associated with weak localization in more conventional metals and semiconductors. The main finding of our work is that the non-zero voltage bias destroys the weak localization contribution in graphene, by introducing a voltage-dependent dephasing time (τ_v). The voltage-induced dephasing process arises from the fact that the wave packets traversing the closed scattering

loops have an energy spread which leads to a decreased efficiency of the constructive interference from which the weak localization emerges.

Acknowledgments

We thank J. Han for useful discussions. This work was supported by Vetenskapsrådet. JPB and GH acknowledge sup-

port from the U.S. Department of Energy, Office of Basic Energy Sciences, Division of Materials Sciences and Engineering (DE-FG02-04ER46180), while HR is grateful for support from the National Science Foundation (ECCS-1509221). RS acknowledges support from the Thailand Research Fund (contract # TRG5880012).

-
- [1] G. Bergmann, Phys. Rev. B **28**, 2914 (1983).
 - [2] G. Bergmann, Phys. Rep. **107**, 1 (1984).
 - [3] P. A. Lee and T. V. Ramakrishnan, Rev. Mod. Phys. **57**, 287 (1985).
 - [4] E. McCann, K. Kechedzhi, V. I. Fal'ko, H. Suzuura, T. Ando, and B. L. Altshuler, Phys. Rev. Lett. **97**, 146805 (2006).
 - [5] D. V. Khveshchenko, Phys. Rev. Lett. **97**, 036802 (2006).
 - [6] A. F. Morpurgo and F. Guinea, Phys. Rev. Lett. **97**, 196804 (2006).
 - [7] K. Kechedzhi, V. I. Fal'ko, E. McCann, and B. L. Altshuler, Phys. Rev. Lett. **98**, 176806 (2007).
 - [8] X.-Zh. Yan and C. S. Ting, Phys. Rev. Lett. **101**, 126801 (2008).
 - [9] M.O. Nestoklon, N.S. Averkiev, S.A. Tarasenko, Sol. St. Comm. **151**, 1550 (2011).
 - [10] E. McCann and V. I. Fal'ko, Phys. Rev. Lett. **108**, 166606 (2012).
 - [11] S. V. Morozov, K. S. Novoselov, M. I. Katsnelson, F. Schedin, L. A. Ponomarenko, D. Jiang, and A. K. Geim, Phys. Rev. Lett. **97**, 016801 (2006).
 - [12] X. Wu, X. Li, Z. Song, C. Berger, and W. A. de Heer, Phys. Rev. Lett. **98**, 136801 (2007).
 - [13] R. V. Gorbachev, F. V. Tikhonenko, A. S. Mayorov, D. W. Horsell, and A. K. Savchenko, Phys. Rev. Lett. **98**, 176805 (2007).
 - [14] F. V. Tikhonenko, D. W. Horsell, R. V. Gorbachev, and A. K. Savchenko, Phys. Rev. Lett. **100**, 056802 (2008).
 - [15] D.-K. Ki, D. Jeong, J.-H. Choi, H.-J. Lee, and K.-S. Park, Phys. Rev. B **78**, 125409 (2008).
 - [16] T. Shen, Y. Q. Wu, M. A. Capano, L. P. Rokhinson, L. W. Engel, and P. D. Ye, Appl. Phys. Lett. **93**, 122102 (2008).
 - [17] F. V. Tikhonenko, A. A. Kozikov, A. K. Savchenko, and R. V. Gorbachev, Phys. Rev. Lett. **103**, 226801 (2009).
 - [18] J. Eroms and D. Weiss, New J. Phys. **11**, 095021 (2009).
 - [19] J. Berezovsky and R. M. Westervelt, Nanotechnol. **21**, 274014 (1998).
 - [20] Y.-F. Chen, M.-H. Bae, C. Chialvo, T. Dirks, A. Bezryadin and N. Mason, J. Phys.: Condens. Matt. **22**, 205301 (2010).
 - [21] Q. Yu, L. A. Jauregui, W. Wu, R. Colby, J. Tian, Z. Su, H. Cao, Z. Liu, D. Pandey, D. Wei, T. F. Chung, P. Peng, N. P. Guisinger, E. A. Stach, J. Bao, S.-S. Pei and Y. P. Chen, Nat. Mater. **10**, 443 (2011).
 - [22] F. Oberhuber, S. Blien, S. Heydrich, F. Yaghobian, T. Korn, C. Schuller, C. Strunk, D. Weiss, and J. Eroms, Appl. Phys. Lett. **103**, 143111 (2013).
 - [23] T. Ando, T. Nakanishi, and R. Saito, J. Phys. Soc. Jpn. **67**, 2857 (1998).
 - [24] T. Ando, J. Phys. Soc. Jpn. **74**, 777 (2005).
 - [25] G.J. Dolan and D.D. Osherof, Phys. Rev. Lett. **43**, 721 (1979).
 - [26] H. Hoffman, F. Hofmann and W. Schoepe, Phys. Rev. B **25**, 5563 (1982).
 - [27] H. Linke, P. Omling, H. Xu, and P. E. Lindelof, Phys. Rev. B, **55**, 4061 (1997).
 - [28] H. B. Weber, R. Häussler, and H. v. Löhneysen, Phys. Rev. B, **63**, 165426 (2001).
 - [29] A. S. Price, S. M. Hornett, A. V. Shytov, E. Hendry, and D. W. Horsell, Phys. Rev. B **85**, 161411(R) (2012).
 - [30] A. M. R. Baker, J. A. Alexander-Webber, T. Altbauer, S. D. McMullan, T. J. B. M. Janssen, A. Tzalenchuk, S. Lara-Avila, S. Kubatkin, R. Yakimova, C.-T. Lin, L.-J. Li, and R. J. Nicholas, Phys. Rev. B **87**, 045414 (2012).
 - [31] L. P. Gor'kov, A. I. Larkin, and D. E. Khmel'nitskiĭ, JETP Lett. **30**, 228 (1980).
 - [32] B.L. Altshuler, A.G. Aronov, D.E. Khmel'nitskii, and A.I. Larkin, in *Quantum Theory of Solids*, edited by I.M. Lifshits (Mir, Moscow, 1982).
 - [33] S. Chakravarty and A. Schmid, Phys. Rep. **140**, 193 (1986).
 - [34] N. H. Shon and A. Ferraz, Sol. State Comm. **86**, 195 (1993).
 - [35] H. Haug and A. -P. Jauho, *Quantum Kinetics in Transport and Optics of Semi-Conductors* (Springer-Verlag, Berlin – Heidelberg – New York, 1998).
 - [36] J. J. Lin and J. P. Bird, Journal of Physics: Condensed Matter **14**, R501 (2002).
 - [37] R. R. Biswas and A. V. Balatsky, Phys. Rev. B, **81**, 233405 (2010).
 - [38] J.-H. She, J. Fransson, A. R. Bishop, and A. V. Balatsky, Phys. Rev. Lett. **110**, 026508 (2013).
 - [39] J. Fransson, A. Black-Schaffer, and A. V. Balatsky, Phys. Rev. B **94**, 075401 (2016).
 - [40] G. Bergmann, Phys. Rep. **107**, 1 (1983).
 - [41] S. Lee, N. Wijesinghe, C. Diaz-Pinto, and H. Peng, Phys. Rev. B, **82**, 045411 (2010).
 - [42] A. S. Price, S. M. Hornett, A. V. Shytov, E. Hendry, and D. W. Horsell, Phys. Rev. B, **85**, 161411(R) (2012).
 - [43] P. A. Lee, A. D. Stone, and H. Fukuyama, Phys. Rev. B, **35**, 1039 (1987).
 - [44] N. M. R. Peres, F. Guinea, and A. H. Castro Neto, Phys. Rev. B **73** 125411 (2006).
 - [45] B. L. Altshuler, D. Khmel'nitski, A. I. Larkin, and P. A. Lee, Phys. Rev. B **22**, 5142 (1980).
 - [46] T. O. Wehling, A. V. Balatsky, M. I. Katsnelson, A. I. Lichtenstein, K. Scharnberg, and R. Wiesendanger, Phys. Rev. B, **75**, 125425 (2007).
 - [47] S. H. M. Jafri, K. Carva, E. Widenkvist, T. Blom, B. Sanyal, J. Fransson, O. Eriksson, U. Jansson, H. Grennberg, O. Karis, R. A. Quinlan, B. C. Holloway, and K. Leifer, J. Phys. D: Appl. Phys. **43**, 045404 (2010).
 - [48] H. Hammar, P. Berggren, and J. Fransson, Phys. Rev. B, **88**, 245418 (2013).
 - [49] R. Somphonsane, H. Ramamoorthy, G. He, J. Nathawat, C.-P. Kwan, Y.-H. Lee, J. Fransson, and J. P. Bird, arXiv:1610.xxxxx.